Journal of Power Sources 211 (2012) 133–139

Contents lists available at SciVerse ScienceDirect

Journal of Power Sources

journal homepage: www.elsevier.com/locate/jpowsour

Improving electrochemical properties of spinel lithium titanate by incorporation of titanium nitride *via* high-energy ball-milling

Jiwei Zhang [1], Jingwei Zhang [1], Wei Cai, Fenli Zhang, Laigui Yu, Zhishen Wu, Zhijun Zhang*

Key Laboratory for Special Functional Materials of Ministry of Education, Henan University, Kaifeng 475004, PR China

ARTICLE INFO

Article history:
Received 25 January 2012
Received in revised form
2 March 2012
Accepted 15 March 2012
Available online 10 April 2012

Keywords:
High-energy ball-milling
Spinel lithium titanate
Titanium nitride
Nanocomposite
Lithium-ion batteries
Anode material

ABSTRACT

$Li_4Ti_5O_{12}$/TiN nanocomposites are fabricated through high-energy ball-milling of the mixture of spinel lithium titanate and TiN powder with different mass ratios of 100:1, 100:2, 100:4, and 100:8 (resultant nanocomposites are denoted as LTO–TiN-1B, LTO–TiN-2B, LTO–TiN-4B, and LTO–TiN-8B). All ball-milled samples exhibit markedly improved electrochemical properties than pristine $Li_4Ti_5O_{12}$. Particularly, LTO–TiN-2B electrode has a high capacity of 130 mA h g^{-1} at a charge/discharge rate of 20C and the capacity retention was 85% after 1000 cycles at 10C, showing the best electrochemical performance and great potential as an anode material for high-rate lithium-ion batteries. The transmission electron microscopy and X-ray diffraction results indicate that amorphous TiN is generated on the surface of LTO. The improved electrochemical performance may be attributed to TiN which can significantly enhance the electronic conductivity of the nanocomposites.

1. Introduction

In recent years, spinel lithium titanate ($Li_4Ti_5O_{12}$, LTO) has attracted considerable attention as an alternative anode material for lithium-ion batteries [1–6], because it has a very flat potential plateau at approximately 1.5 V versus Li^+/Li and displays good reversibility and structural stability (zero-strain insertion material) in the charge/discharge process. In the meantime, $Li_4Ti_5O_{12}$ has a better thermal stability than natural graphite [7] and a one order of magnitude larger chemical diffusion coefficient than carbonaceous anode materials, which should be favorable for high rate operation [8]. However, $Li_4Ti_5O_{12}$ has a poor electrical conductivity ($<10^{-13}$ S cm^{-1}) leading to initial capacity loss and poor rate capability [9], which greatly limits its practical applications. To overcome this drawback and improve the electrochemical performance and increase the lithium ionic conductivity of $Li_4Ti_5O_{12}$, researchers have made great efforts to synthesize various specially-shaped nanostructured $Li_4Ti_5O_{12}$ (e.g., hollow-sphere [10], nanotube [11], and three-dimensionally ordered macropore [12]), to substitute a small quantity of Li^+, Ti^{4+} or O^{2-} sites with supervalent metal ions (e.g., V^{5+} [13], Mo^{4+} [14], Cr^{3+} [15], Ni^{3+} [16], and Br^- [17]) and to incorporate second phase with high electronic conductivity (e.g., Cu [18], Ag [19], carbon [20,21], carbon nanotube [22], graphene [23], SnO_2 [24], and organic compounds [25]). Recently, DeSisto et al. [26], by making use of atomic layer deposition technique, prepared lithium titanate powder coated with TiN layer and obtained improved electrochemical performance. Park et al. [27] and Zhou et al. [28], who separately prepared $Li_4Ti_5O_{12}$/TiN nanocomposites by annealing $Li_4Ti_5O_{12}$ in flowing NH_3 gas, attributed the excellent electrochemical properties of $Li_4Ti_5O_{12}$/TiN at high current densities to the formation of amorphous TiN with metallic conductivity on the surface of $Li_4Ti_5O_{12}$. Unfortunately, ammonia used in those researches is dangerous, corrosive and environmentally unfriendly, making it infeasible to achieve large-scale production. Zhang et al. [29] selected urea as a nitrogen source to prepare a TiN layer with high electrical conductivity on $Li_4Ti_5O_{12}$ through heat-treatment and obtained greatly improved electrochemical rate performance and cycling behavior than raw $Li_4Ti_5O_{12}$. This approach, however, relies on calcination at elevated temperature of 800 °C to coat TiN on the surface of $Li_4Ti_5O_{12}$; and as-obtained $Li_4Ti_5O_{12}$/TiN nanocomposite has only slightly increased discharge specific capacity owing to large average size of about 200 nm. This means it still remains a challenge to develop a facile and scalable process to prepare $Li_4Ti_5O_{12}$/TiN nanocomposites without using expensive equipment as well as dangerous and highly corrosive medium like ammonia.

* Corresponding author. Tel./fax: +86 378 3881358.
E-mail address: zzj391@yahoo.cn (Z. Zhang).
[1] The first two authors contributed equally to this paper.

0378-7753/$ – see front matter © 2012 Elsevier B.V. All rights reserved.
doi:10.1016/j.jpowsour.2012.03.088

Bearing those perspectives in mind, in the present research we pay special attention to preparing $Li_4Ti_5O_{12}$/TiN nanocomposite by high-energy ball-milling method. High-energy ball-milling, as a mechanical chemical method, uses mechanical energy to induce chemical reaction and change in material organization, structure and property *via* high-speed vibration and rotation, making it feasible to fabricate materials with special structure that is hard to produce by other technique thereby extending the utilization range of materials. For instances, Foster et al. prepared nanocomposite of lithium oxide and tin by reducing SnO with Li_3N through a powder milling process; and they found that the tin particles were uniformly distributed within a lithium oxide matrix with the majority of tin particles on the order of 100 nm or less and most of the irreversible capacity on the first cycle associated with SnO electrodes was eliminated [30]. Ni et al. prepared $LiMnPO_4$ by applying a high-energy ball-milling method and found that ball-milling process led to decreased crystallinity and particle size in association with expanded unit cell volume and lattice defects of $LiMnPO_4$. As a result, the lattice stress and strain associated with Jahn–Teller distortion were more readily relaxed, resulting in remarkably improved electrochemical activity of ball-milled $LiMnPO_4$ than the pristine one [31]. Tu et al. synthesized nano-sized $LiFePO_4$/C composite by making use of ball-milling route and follow-up solid-state reaction, acquiring excellent rate capability and cycling stability [32]. Enlightened by those researches, here we report the preparation of $Li_4Ti_5O_{12}$/TiN nanocomposite by high-energy ball-milling as well as investigation of the microstructure and electrochemical properties of as-prepared nanocomposite product in relation to pristine $Li_4Ti_5O_{12}$. This, to the best of our knowledge, is the first report on high-energy ball-milled $Li_4Ti_5O_{12}$/TiN nanocomposite.

2. Experimental

2.1. Sample preparation

$Li_4Ti_5O_{12}$ particles with a spinel structure were synthesized by aqueous ion-exchange, where the solution of 0.6 M LiOH containing sodium titanate nanotubes (the preparation of sodium titanate nanotubes has been reported elsewhere [33]) at a Li to Ti molar ratio of 6:1 was used. The mixture was stirred at room temperature for 24 h, followed by filtrating and drying at 60 °C for 12 h. The dried mixture was then heated at 600 °C for 2 h in air and cooled down to room temperature naturally, yielding spinel $Li_4Ti_5O_{12}$ denoted as LTO. As-synthesized LTO was mixed with TiN powder (purchased from Alfa) at a mass ratio of 100:1, 100:2, 100:4 and 100:8, respectively. Resultant LTO–TiN mixtures were sealed in an 80 mL agate mortar and placed in an argon-filled glove box, followed by 10 h of ball-milling with a Planetary Mono Mill P-6 (Fritsch, Germany) at a rotary rate of 350 rev min^{-1}, where the ball-miller was shut down for an interval of 15 min every 1 h. Corresponding ball-milled mixtures are denoted as LTO–TiN-1B, LTO–TiN-2B, LTO–TiN-4B, and LTO–TiN-8B, respectively (here numerals 1, 2, 4, and 8 refer to mass ratio 100:1, 100:2, 100:4 and 100:8 of pristine LTO to TiN powder; letter B refers to ball-milling). In the meantime, pristine LTO was also mixed with TiN at a mass ratio of 100:8 and ground with hand, yielding sample denoted as LTO–TiN-8M for a comparative study.

Besides, a proper amount of glucose was dissolved in distilled water and mixed with as-obtained LTO at a mass ratio of 100:2 (versus the amount of carbon, i.e., the mass ratio of LTO to C). Resultant mixture was heated at 60 °C to allow full drying. Finally, as-dried mixture was calcinated at 600 °C for 2 h under Ar atmosphere, generating target $Li_4Ti_5O_{12}$/C composite denoted as LTO/C for a comparative study.

2.2. Characterization

Scanning electron microscopic (SEM) images of samples were obtained using a JOEL JSM 6701 at a beam potential of 5 kV. Transmission electron microscopic (TEM) pictures were obtained using a JEM-2010 electron microscope. X-ray diffraction (XRD) patterns were measured with a Philips X'Pert Pro X-ray diffractometer. An ESCA-LAB210 X-ray photoelectron spectroscope (XPS) was performed to determine the surface composition and valence states of typical elements of various ball-milled samples, where the binding energy of contaminant carbon (C1s: 284.8 eV) was adopted to calibrate XPS data.

2.3. Electrochemical measurements

The mixture of active materials (pristine LTO or $Li_4Ti_5O_{12}$/TiN nanocomposites), conductive agent (carbon black), and binder (polyvinylidene fluoride, abridged as PVDF) with a mass ratio of 80:10:10 was dissolved in *N*-methyl-2-pyrrolidone and coated onto copper foils. As-coated copper foils were dried under vacuum at 120 °C for 12 h, cut into plates with a size of about 15 mm, and pressed into working electrodes. The working electrodes and metallic Li counter electrode were assembled into cells by using Celgard 2400 as the separator and 1 M solution of $LiPF_6$ in ethylene carbonate and dimethyl carbonate (volume ratio 1:1) as the electrolyte. The cells were constructed in an Ar-filled glove box. The charge/discharge curves were measured using a LAND Cell tester (Wuhan, China) at a cutoff voltage of 1.0–3.0 V. Cyclic voltammetric curves were recorded in a voltage range of 1.0–2.2 V at a scan rate of 0.1 mV s^{-1}. An IM6 impedance and electrochemical measurement system with a conventional two-electrode cell (Zahner, Germany) was performed to measure the electrochemical impedance spectra (EIS). Alternating current amplitude of 5 mV was applied, and data were collected in a frequency range from 0.01 Hz to 100 kHz.

3. Results and discussion

3.1. Characterization of $Li_4Ti_5O_{12}$/TiN nanocomposite

Fig. 1 shows the TEM (a) and SEM (b, c) images of various samples. Pristine TiN has a sheet-like morphology at micron scale (Fig. 1a), being about 0.5–3.0 μm. Micron scale TiN sheets still exist in the LTO–TiN-8M sample (Fig. 1b), because it only experiences a simple grinding process. However, original sheet-like micron-sized TiN particulates are not observed in ball-milled LTO–TiN-2B (Fig. 1c), which indicates that the size of TiN particulates is greatly reduced after ball milling, possibly due to continuous mechanical deformation during ball-milling process resulting in grain refinement. High-resolution TEM (HRTEM) image (Fig. 1d) indicates that sample LTO–TiN-2B has a highly ordered lattice structure and a spacing of 0.45 nm which corresponds to the interplanar spacing of the (111) plane of spinel LTO. Besides, sample LTO–TiN-2B has a glassy surface structure with a thickness of a few nanometers, which is much different from that of the core and is due to the formation of amorphous TiN layer on the surface of LTO. The amorphous TiN in sample LTO–TiN-2B is generated *via* crystal-to-amorphous phase transition of micron-sized TiN induced by high-energy-ball-milling [34,35]. Namely, micron-sized TiN sheets experience grain refinement under continuous shear stress and impact force attributed to ball-to-ball and ball-to-vial-wall collisions; and excessive free enthalpy produced in continued high-energy ball-milling is accumulated at the nano-grain boundary. As a result, micro-sized TiN sheets undergo crystal-to-amorphous phase transition yielding amorphous TiN with a high electrical

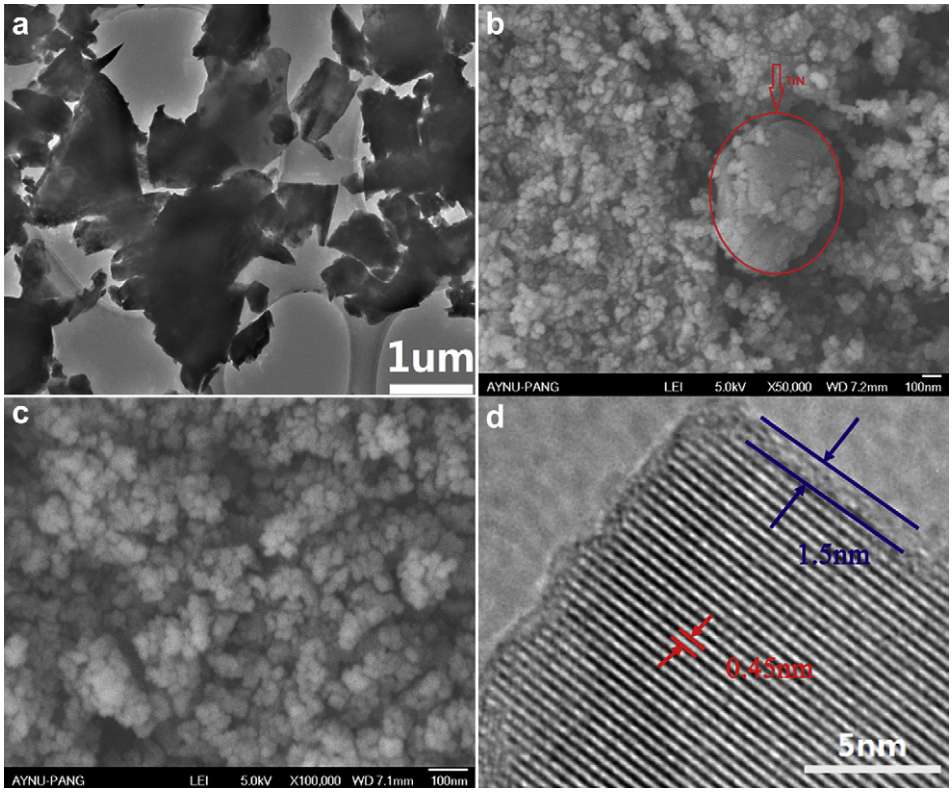

Fig. 1. (a) TEM image of pristine TiN; (b) SEM image of LTO–TiN-8M; (c) SEM image of LTO–TiN-2B and (d) high-resolution TEM image of LTO–TiN-2B.

conductivity on the surface of LTO. In this way, LTO/TiN nanocomposites with good electrical conductivity can be prepared *via* a facile and scalable process at lowered temperature without using expensive equipments or dangerous and highly corrosive ammonia.

The XRD patterns of various as-synthesized $Li_4Ti_5O_{12}$/TiN nanocomposites are shown in Fig. 2. It can be seen that pristine LTO has cubic spinel structure and contains no impurities, and its crystal structure is retained after high-energy ball-milling. In the meantime, samples LTO–TiN-1B and LTO–TiN-2B do not show any diffraction peaks of TiN, possibly because they contain too low content of TiN. Samples LTO–TiN-4B and LTO–TiN-8B, however, show XRD peaks of TiN labeled by asterisks (*) along with those of LTO. This implies that mixing LTO and TiN powder at a mass ratio of 100:4 and above facilitates the detection of TiN in high-energy ball-milled sample by XRD. The mean crystallite sizes of pristine LTO and LTO/TiN nanocomposites, calculated by Scherrer's formula, are all about 19 ± 1 nm. Moreover, by comparing the XRD pattern of LTO–TiN-8B with that of LTO–TiN-8M, we can see that the diffraction peaks of TiN in the former are broader and weaker than those of TiN in the later, which implies that both the crystallinity and crystalline size of TiN are greatly reduced during high-energy ball-milling, due to ball-milling-induced grain refinement and crystal-to-amorphous phase transition of TiN.

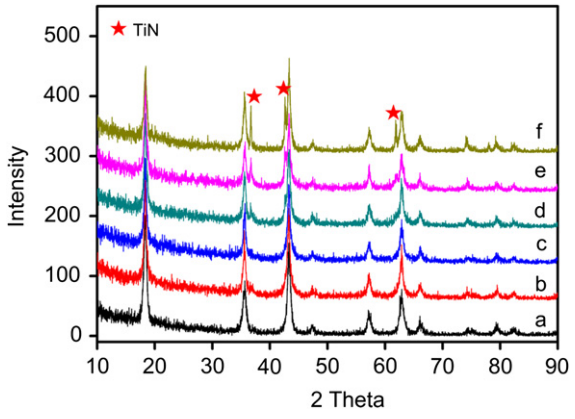

Fig. 2. XRD patterns of (a) pristine LTO, (b) LTO–TiN-1B, (c) LTO–TiN-2B, (d), LTO–TiN-4B, (e) LTO–TiN-8B, and (f) LTO–TiN-8M.

XPS techniques were utilized to test whether there is any new chemical bond produced or there is change in chemical environment of surface elements. As shown in Fig. 3, two kinds of N species (N1s spectrum) are detected in sample LTO–TiN-8M, corresponding to N1s binding energies of 396.3 eV and 399.5 eV. The N1s peak at 396.3 eV corresponds to Ti–N–Ti bond [36,37]; and that at 399.5 eV can be assigned to Ti–N–O bond [36,37] formed by surface oxidation of TiN. As to sample LTO–TiN-8B, it can be seen that high-energy ball-milling of the mixture of LTO and TiN generates a new N1s peak around 402.0 eV. This new N1s peak can be assigned to Li_3N [38], and it is originated from the chemical reaction between N and Li under elevated local temperature, increased reaction interface area associated with repeated fracture and rewelding of powders, and enhanced diffusion rate of atoms in ball-milling process. In other words, Li_3N as one of the best lithium-ion conducting compounds ($\sigma_{Li+} \approx 10^{-4}$ S cm^{-1} at room temperature and $D_{Li} \approx 10^{-3}$ cm^2 s^{-1} at 500 °C) [39,40] is conducive to diffusion and transmission of lithium ions in the electrode. The TiN/Li_3N ratio of sample LTO–TiN-8B was calculated, based on the deconvolution of the N1s XPS spectrum, to be about 6.3:1. This means that N mainly exists as titanium nitride in sample LTO–TiN-8B, but a small part of N exists as lithium nitride in the nanocomposite.

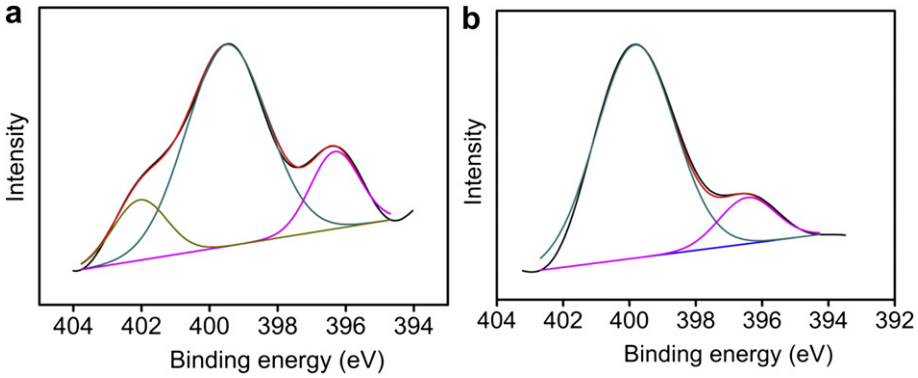

Fig. 3. XPS spectrum of N1s of (a) LTO–TiN-8B and (b) LTO–TiN-8M.

3.2. Electrochemical properties of $Li_4Ti_5O_{12}$/TiN nanocomposite

Fig. 4 shows the first charge/discharge curves of pristine LTO and LTO–TiN-2B electrodes at different rates from 1C to 20C. Both electrodes exhibit a flat operation potential plateau when they are charged/discharged at low rates such as 0.5C and 3C (Fig. 4a). However, with the increase of rate, the potential plateau of pristine LTO becomes shorter and gradually bends down to almost zero level; but that of LTO–TiN-2B electrode still remains flat even at a high rate of 20C (Fig. 4b). This is because, at an increased rate, the polarization of pristine LTO is increased in the absence of ball-milled TiN powder. The potential difference of the two electrodes is comparatively shown in Fig. 4c where the difference between the charge and discharge plateau potentials can reflect the degree of polarization of the electrode. The potential differences for LTO–TiN-2B electrode are much smaller than those of pristine LTO electrode at all discharge rates from 0.5C to 20C. This again indicates that the ball-milled electrode has lower polarization and better reaction kinetics, due to improved electrical conductivity and lithium ion diffusion of the mixture of LTO and TiN powder during high-energy ball-milling. In addition, a comparison of the first discharge/charge curves of pristine LTO and LTO–TiN-2B electrode at 0.5C (Fig. 4d) demonstrates that, aside from the two-phase insertion reaction, single-phase insertion reaction of $Li_{4+\delta}Ti_5O_{12}$ (or $Li_{7-\gamma}Ti_5O_{12}$) takes place at the beginning (or end) of the discharge curve; and LTO–TiN-2B electrode has a broadened single phase region than pristine LTO electrode, possibly due to the formation of locally modified amorphous TiN near to the surface of LTO. Considering that the main contribution of single phase to the rate performance should be not only the improved electronic conductivity but also the improved ionic conductivity (or Li-ion mobility) [1], we suppose that the improved rate performance of LTO–TiN-2B electrode as compared with LTO electrode is attributed to the formation of amorphous TiN on the surface of LTO leading to improved electronic conductivity.

Fig. 5a shows the rate performance of pristine LTO and various ball-milled LTO–TiN mixtures. It can be seen that all the ball-milled LTO–TiN samples possess better rate performance than pristine

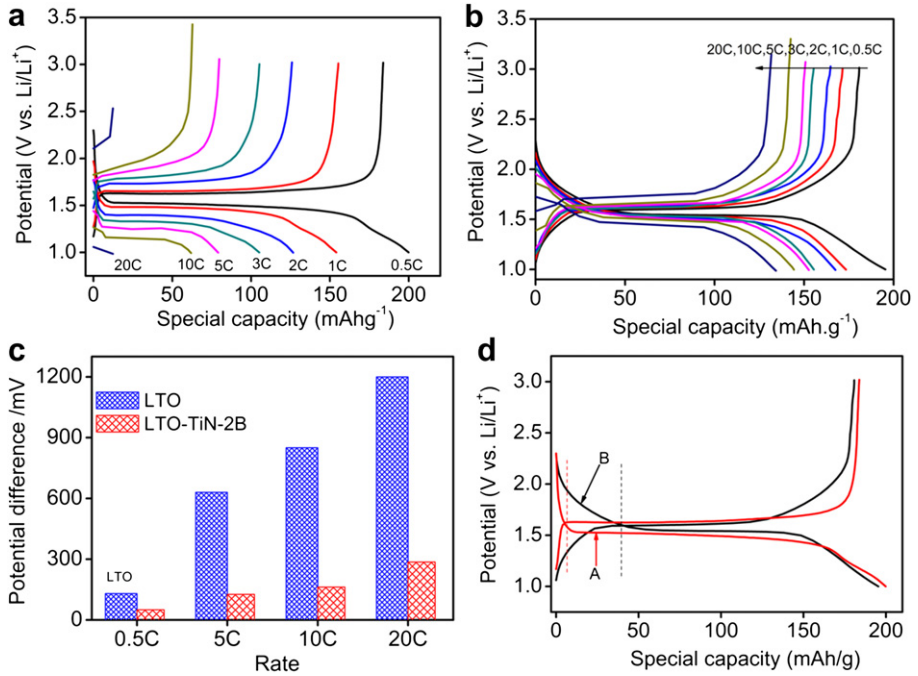

Fig. 4. Charge/discharge curves of (a) pristine LTO and (b) LTO–TiN-2B. (c) Comparison of the charge/discharge plateau potential difference. (d) Comparison of the charge/discharge curves of (A) pristine LTO and (B) LTO–TiN-2B at 0.5C.

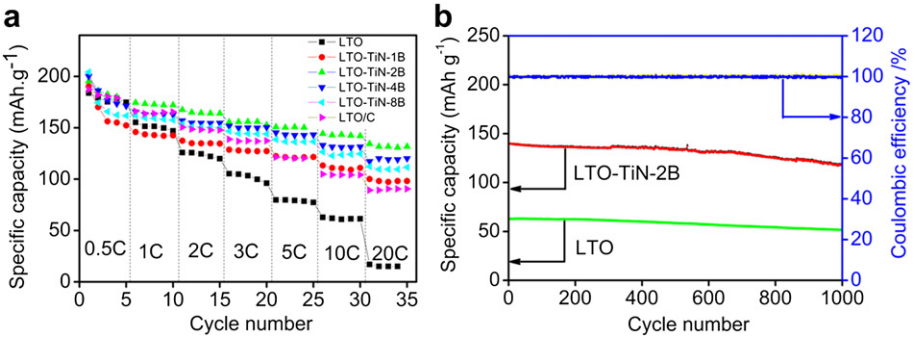

Fig. 5. (a) Rate performance of various electrodes and (b) cyclic performance of pristine LTO and LTO–TiN-2B electrodes at 10C.

LTO within the tested rate range. At a low current density of 0.5C, the specific capacities of the ball-milled samples are similar to that of pristine LTO; but the specific capacity of pristine LTO fades rapidly with increasing rate. Different from LTO, all the ball-milled samples show excellent rate-capability even at a high charge/discharge current density of 20C; and in particular, sample LTO–TiN-2B possesses the maximum specific capacity of 130 mA h g^{-1}, which is 10 times as much as that of pristine LTO and the high rate performance is also superior to carbon-coated $Li_4Ti_5O_{12}$ (Fig. 5a), which pristine LTO prepared by the similar conductions. This can also be attributed to amorphous TiN (with a metallic conductivity as much as 1×10^6–4×10^6 S m^{-1}, far higher than that of graphite carbon) formed on the surface of $Li_4Ti_5O_{12}$ [29]. The specific capacity of sample LTO–TiN-2B at 20C is not only much greater than that of TiN-coated spinel LTO nanostructures measured at lowered rate (3–10C) [27–29] but also greater than or at least comparable to that of previously reported carbon-modified $Li_4Ti_5O_{12}$. For example, $Li_4Ti_5O_{12}$/graphene hybrid materials have a specific capacity of 130 mA h g^{-1} at 20C [41], carbon-coated nanosized $Li_4Ti_5O_{12}$ has a specific capacity of 126 mA h g^{-1} at 20C [42,43], and multi-walled carbon nanotube@$Li_4Ti_5O_{12}$ coaxial nanocables have a specific capacity of 123.6 mA h g^{-1} at 20C [44]. In the meantime, sample LTO–TiN-2B has a capacity retention rate of 75% at 20C as compared with the capacity at 0.5C as a standard. Fig. 5b shows the cycle behavior of LTO–TiN-2B electrode as an example. It can be seen that the electrode has a stable cycle life and the capacity retention of 85% after 1000 cycles at high charge/discharge rate of 10C; and its columbic efficiency is approximately 100% throughout the cycling, which means that the lithium intercalation and release are well reversible.

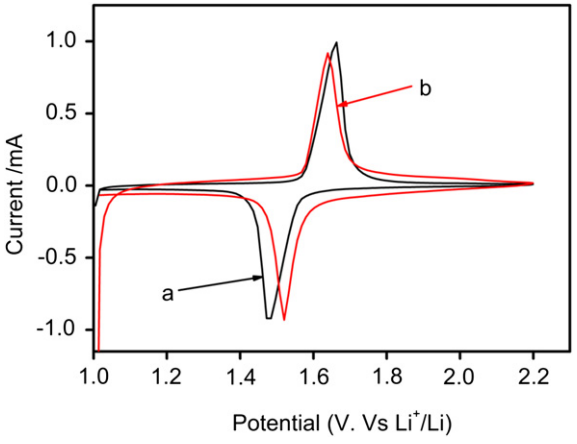

Fig. 6. Cyclic voltammograms of (a) pristine LTO and (b) LTO–TiN-2B.

The cyclic voltammograms of LTO and LTO–TiN-2B are shown in Fig. 6. One pair of cathodic/anodic peaks is observed for both samples, corresponding to a cathodic and anodic process. Moreover, no other redox peaks are observed in the cyclic voltammograms, which indicates that the incorporation of TiN power does not change the electrochemical reaction process of LTO in the tested voltage range. Table 1 presents the position and peak current ratio of oxidation and reduction peaks of various electrodes determined by cyclic voltammograms. Pristine LTO shows a cathodic peak around 1.48 V and an anodic peak around 1.66 V, corresponding to Li intercalation and deintercalation; and the difference between the cathodic and anodic peak potentials is about 0.18 V. After being ball-milled together with TiN power, the difference between the cathodic and anodic peak potentials of various ball-milled $Li_4Ti_5O_{12}$/TiN electrodes is reduced. The potential difference between anodic and cathodic peaks can reflect the polarization degree of the electrodes. Particularly, electrode LTO–TiN-2B shows the lowest potential difference among the tested ball-milled $Li_4Ti_5O_{12}$/TiN electrodes, meaning it is most weakly polarized; and its ratio of anodic peak current (I_{pa}) to cathodic peak current (I_{pc}), I_{pa}/I_{pc}, is nearly equal to 1 (0.99). This demonstrates that Li ions intercalate and deintercalate reversibly in the redox system which remains in equilibrium throughout the potential scan, corresponding to the excellent rate capability of the ball-milled samples.

To clarify why the ball-milled samples deliver weak electrochemical polarization, we applied alternating current EIS technique to examine the kinetic process of the electrode reactions. Fig. 7 shows the impedance spectra of LTO electrode and ball-milled $Li_4Ti_5O_{12}$/TiN electrodes during discharging to 1.0 V at room temperature. The Nyquist plots of all tested electrodes show a semicircle at the high frequency region and a sloping line at the low frequency region. The impedance plots were fitted using the equivalent circuit model (the inset in Fig. 7; where R_0 corresponds to the ohmic resistance of the cell mainly contributed from the electrolyte and electrode, and it is obtained from the high frequency intercept of the semicircle with the real axis; C_d and R_{ct} represent the double-layer capacitance and charge-transfer

Table 1
Position and peak current ratio of oxidation and reduction peaks of various electrodes.

Sample	Position of peaks/V		Potential difference ΔV	Peak height ratio I_{pa}/I_{pc}
	Oxidation	Reduction		
LTO	1.66	1.48	0.18	1.06
LTO–TiN-1B	1.65	1.51	0.14	0.96
LTO–TiN-2B	1.64	1.52	0.12	0.99
LTO–TiN-4B	1.65	1.51	0.14	1.07
LTO–TiN-8B	1.64	1.52	0.12	1.07

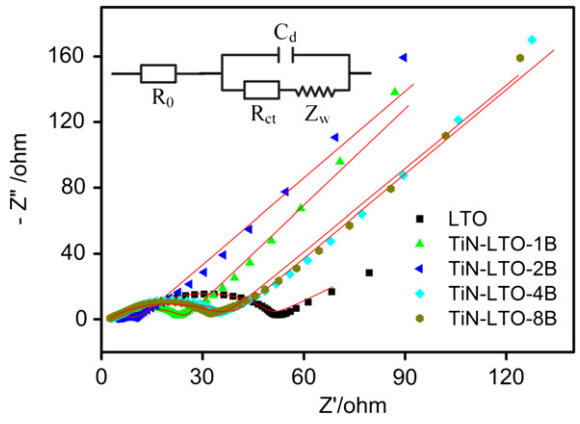

Fig. 7. Electrochemical impedance spectra of various electrodes. The red line is the fitting results. (For interpretation of the references to colour in this figure legend, the reader is referred to the web version of this article.)

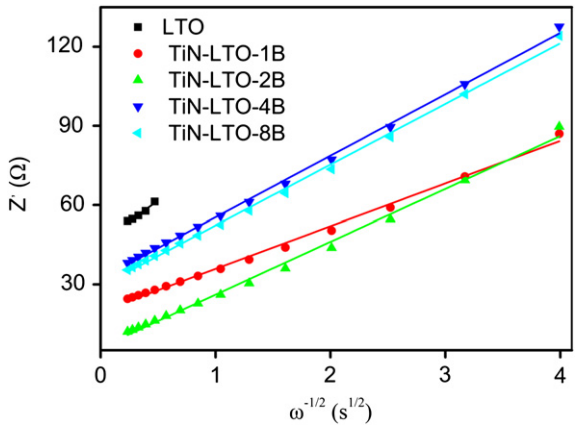

Fig. 8. Graph of Z' plotted against $\omega^{-1/2}$ at low frequency region for pristine LTO and ball-milled electrodes.

resistance, corresponding to the semicircle at medium frequency; and Z_w is the Warburg impedance arising from the semi-infinite diffusion of Li^+ ions in electrode, corresponding to the inclined straight line in low frequencies). The impedance parameters R_0 and R_{ct} of all electrodes, derived using equivalent circuit model, are listed in Table 2. It can be seen that the fitted data are in good agreement with the experimental ones. The lithium-ion diffusion coefficient (D) is calculated according to the following equation [45]:

$$D = R^2T^2/2A^2n^4F^4C^2\sigma^2 \quad (1)$$

where R is the gas constant, T is the absolute temperature, A is the surface area of the electrode, n is the number of electrons transferred in the half-reaction for the redox couple, F is the Faraday constant, C is the concentration of Li ion in solid, and σ is the Warburg factor which is obtained from the slope of Z' *vs.* reciprocal square root of frequency in the low-frequency region ($\omega^{-1/2}$; as shown in Fig. 8). The lithium diffusion coefficients (D) for pristine LTO and ball-milled $Li_4Ti_5O_{12}$/TiN electrodes were calculated from the results shown in Table 2. Ball-milling-induced TiN and Li_3N have different influences on the electrochemical performance. Namely, similar to metals, TiN possesses good electrical conductivity and can reduce the interfacial charge transfer resistance; and Li_3N has high ion conductivity and is conducive to diffusion and transmission of lithium ions in the electrode. As can be seen clearly in Table 2, high-energy ball-milling leads to greatly decreased charge transfer resistance and increased lithium diffusion coefficients, due to ball-milling-induced formation of amorphous TiN with high electrical conductivity on the surface of $Li_4Ti_5O_{12}$ and generation of Li_3N phase with good lithium ion conducting ability. Thus we suppose that the present approach can be well applied for facile and scalable production of $Li_4Ti_5O_{12}$/TiN nanocomposites with significantly improved electrochemical performance.

Table 2
Impedance parameters derived using equivalent circuit model and lithium diffusion coefficient D for pristine LTO and ball-milled electrodes.

Sample	R_0 (Ω)	R_{ct} (Ω)	D ($cm^2\ s^{-1}$)
LTO	6.1	51.1	0.64×10^{-12}
LTO–TiN-1B	2.5	23.6	2.3×10^{-12}
LTO–TiN-2B	3.7	11.0	1.5×10^{-12}
LTO–TiN-4B	2.1	36.8	1.1×10^{-12}
LTO–TiN-8B	2.5	34.7	1.2×10^{-12}

4. Conclusions

$Li_4Ti_5O_{12}$/TiN nanocomposites with different compositions have been prepared by high-energy ball-milling of the mixtures of $Li_4Ti_5O_{12}$ and TiN powder with different mass ratios. As-synthesized balled milled $Li_4Ti_5O_{12}$/TiN nanocomposites possess much better high rate performance than pristine $Li_4Ti_5O_{12}$, which is closely related to ball-milling-induced formation of amorphous TiN on the surface of $Li_4Ti_5O_{12}$ and generation of Li_3N phase with good lithium ion conducting ability. Specifically, electrode LTO–TiN-2B possesses the lowest cathodic and anodic peak potential difference; and it shows the maximum specific capacity of 130 mA h g^{-1} even at high charge/discharge rate of 20C and a capacity retention of 85% after 1000 cycles at charge/discharge rate of 10C, showing promising application as an anode material for high-rate lithium ion batteries.

Acknowledgments

We acknowledge the financial support from National Natural Science Foundation of China (Grant Nos. 50902045/E0213 and 20971037/B0111), Foundation of Scientific Committee of Henan Province of China (Grant No. 082102270040), Foundation of Educational Committee of Henan Province of China (Grant Nos. 2008A150004 and 2010GGJS-040) and Financial supports from Key Laboratory of Novel Thin Film Solar Cells, Chinese Academy of Sciences. We are also grateful to Dr. Yi Lichao for his help in ball milling.

References

[1] Y.G. Wang, H.M. Liu, K.X. Wang, H. Eiji, Y.R. Wang, H.S. Zhou, J. Mater. Chem. 19 (2009) 6789.
[2] X. Li, M.Z. Qu, Y.J. Huai, Z.L. Yu, Electrochim. Acta 55 (2010) 2978.
[3] A.S. Prakash, P. Manikandan, K. Ramesha, M. Sathiya, J.M. Tarascon, A.K. Shukla, Chem. Mater. 22 (2010) 2857.
[4] M. Vijayakumar, S. Kerisit, K.M. Rosso, S.D. Burton, J.A. Sears, Z.G. Yang, G.L. Graff, J. Liu, J.Z. Hu, J. Power Sources 196 (2011) 2211.
[5] J.Z. Chen, L. Yang, S.H. Fang, Y.F. Tang, Electrochim. Acta 55 (2010) 6596.
[6] C. Lai, Y.Y. Dou, X. Li, X.P. Gao, J. Power Sources 195 (2010) 3676.
[7] X.L. Yao, S. Xie, C.H. Chen, Q.S. Wang, J.H. Sun, Y.L. Li, S.X. Lu, Electrochim. Acta 50 (2005) 4076.
[8] K. Zaghib, M. Simoneau, M. Armand, M. Gauthier, J. Power Sources 81–82 (1999) 300.
[9] C.H. Chen, J.T. Vaughey, A.N. Jansen, D.W. Dees, A.J. Kahaian, T. Goacher, M.M. Thackery, J. Electrochem. Soc. 148 (2001) A102.
[10] C.H. Jiang, Y. Zhou, I. Honmaa, T. Kudo, H.S. Zhou, J. Power Sources 166 (2007) 514.

[11] S.C. Lee, S.M. Lee, J.W. Lee, J.B. Lee, S.M. Lee, S.S. Han, H.C. Lee, H.J. Kim, J. Phys. Chem. C 113 (2009) 18420.
[12] E.M. Sorensen, S.J. Barry, H.K. Jung, J.R. Rondinelli, J.T. Vaughey, K.R. Poeppelmeier, Chem. Mater. 18 (2006) 482.
[13] T.F. Yi, J. Shu, Y.R. Zhu, X.D. Zhu, C.B. Yue, A.N. Zhou, R.S. Zhu, Electrochim. Acta 54 (2009) 7464.
[14] Z. Zhong, Electrochem. Solid-State Lett. 10 (2007) A267.
[15] P. Martln, M.L. Lopez, C. Pico, M.L. Veiga, Solid State Sci. 9 (2007) 521.
[16] A.D. Robertson, L. Trevino, H. Tukamoto, J.T.S. Irvine, J. Power Sources 81–82 (1999) 352.
[17] Y. Qi, Y. Huang, D. Jia, S.J. Bao, Z.P. Guo, Electrochim. Acta 54 (2009) 4772.
[18] S. Huang, Z. Wen, B. Lin, J. Han, X. Xu, J. Alloys Compd. 457 (2008) 400.
[19] S. Huang, Z. Wen, J. Zhang, X. Yang, Electrochim. Acta 52 (2007) 3704.
[20] G.J. Wang, J. Gao, L.J. Fu, N.H. Zhao, Y.P. Wu, T. Takamura, J. Power Sources 174 (2007) 1109.
[21] L. Cheng, J. Yan, G.N. Zhu, J.Y. Luo, C.X. Wang, Y.Y. Xia, J. Mater. Chem. 20 (2010) 595.
[22] X. Li, M.Z. Qu, Z.L. Yu, Solid State Ionics 181 (2010) 635.
[23] L. Shen, C.Z. Yuan, H.J. Luo, X.G. Zhang, S.D. Yang, X.J. Lu, Nanoscale 3 (2010) 572.
[24] Y.Y. Wang, Y.J. Hao, Q.Y. Lai, J.Z. Lu, Y.D. Chen, X.Y. Ji, Ionics 14 (2008) 85.
[25] S.A.A. Muhtaseb, J.A. Ritter, Adv. Mater. 15 (2003) 101.
[26] M.Q. Snyder, S.A. Trebukhov, B. Ravdel, M.C. Wheeler, J. DiCarlo, C.P. Tripp, W.J. DeSisto, J. Power Sources 165 (2007) 379.
[27] K.S. Park, A. Benayad, D.J. Kang, S.G. Doo, J. Am. Chem. Soc. 130 (2008) 14930.
[28] X.L. Zhou, R.A. Huang, C.Z. Wu, B. Yang, Y. Dai, Acta Phys. Chim. Sin. 26 (2010) 3187.
[29] H.Q. Gao, X.Y. Wang, Y. Xin, Z.A. Zhang, Y.Q. Lai, J. LI, Y.X. Liu, J. Inorg. Mater. 25 (2010) 983.
[30] D.L. Foster, J. Wolfenstine, J.R. Read, W.K. Behl, Electrochem. Solid-State Lett. 3 (2000) 203.
[31] J.F. Ni, Y. Kawabe, M. Morishita, M. Watada, T. Sakai, J. Power Sources 196 (2011) 8104.
[32] W.L. Liu, J.P. Tu, Y.Q. Qiao, J.P. Zhou, S.J. Shi, X.L. Wang, C.D. Gu, J. Power Sources 196 (2011) 7728.
[33] J.J. Yang, Z.S. Jin, X.D. Wang, W. Li, J.W. Zhang, S.L. Zhang, Z.J. Zhang, Dalton Trans. 9 (2003) 3898.
[34] A.Y. Yermakov, Y.Y. Yurchikov, V.A. Barinov, Phys. Met. Metall. 52 (1981) 50.
[35] C.C. Koch, O.B. Cavin, C.G. McKamey, J.O. Scarbrough, Appl. Phys. Lett. 43 (1983) l017.
[36] M. Sathish, B. Viswanathan, R.P. Viswanath, C.S. Gopinath, Chem. Mater. 17 (2005) 6349.
[37] F. Peng, L.F. Cai, L. Huang, H. Yu, H.J. Wang, J. Phys. Chem. Sol. 69 (2008) 1657.
[38] D. Ahn, C. Kim, J.G. Lee, B. Park, J. Solid State Chem. 181 (2008) 2139.
[39] E. Bechthold-Schweikert, M. Mali, J. Roos, D. Brinkmann, Phys. Rev. B 30 (1984) 2891.
[40] T. Lapp, S. Skaarup, Solid State Ionics 11 (1983) 97.
[41] Y. Shi, L. Wen, F. Li, H.M. Cheng, J. Power Sources 196 (2011) 8610.
[42] L.F. Shen, C.Z. Yuan, H.J. Luo, X.G. Zhang, L. Chen, H.S. Li, J. Mater. Chem. 21 (2011) 14414.
[43] G.N. Zhu, H.J. Liu, J.H. Zhuang, C.X. Wang, Y.G. Wang, Y.Y. Xia, Energy Environ. Sci. 4 (2011) 4016.
[44] L.F. Shen, C.Z. Yuan, H.J. Luo, X.G. Zhang, K. Xu, F. Zhang, J. Mater. Chem. 21 (2011) 761.
[45] A.J. Bard, L.R. Faulkner, Electrochemical Methods, Wiley, New York, 2001.